

Shape of (101955) Bennu indicative of a rubble pile with internal stiffness

O. S. Barnouin^{1*}, M. G. Daly², E. E. Palmer³, R. W. Gaskell³, J. R. Weirich³, C. L. Johnson^{3,4}, M. M. Al Asad⁴, J. H. Roberts¹, M. E. Perry¹, H. C. M. Susorney⁴, R. T. Daly¹, E. B. Bierhaus⁵, J. A. Seabrook², R. C. Espiritu¹, A. H. Nair¹, L. Nguyen¹, G. A. Neumann⁶, C. M. Ernst¹, W. V. Boynton⁷, M. C. Nolan⁷, C. D. Adam⁸, M. C. Moreau⁶, B. Rizk⁷, C. Y. Drouet D'Aubigny⁷, E. R. Jawin⁹, K. J. Walsh¹⁰, P. Michel¹¹, S. R. Schwartz⁷, R.-L. Ballouz⁷, E. M. Mazarico⁶, D. J. Scheeres¹², J. W. McMahon¹², W. F. Bottke¹⁰, S. Sugita¹³, N. Hirata¹⁴, N. Hirata¹⁵, S.-i. Watanabe^{16,17}, K. N. Burke⁷, D. N. DellaGiustina⁷, C. A. Bennett⁷, D. S. Lauretta⁷ and The OSIRIS-REx Team¹⁸

The shapes of asteroids reflect interplay between their interior properties and the processes responsible for their formation and evolution as they journey through the Solar System. Prior to the OSIRIS-REx (Origins, Spectral Interpretation, Resource Identification, and Security-Regolith Explorer) mission, Earth-based radar imaging gave an overview of (101955) Bennu's shape. Here we construct a high-resolution shape model from OSIRIS-REx images. We find that Bennu's top-like shape, considerable macroporosity and prominent surface boulders suggest that it is a rubble pile. High-standing, north-south ridges that extend from pole to pole, many long grooves and surface mass wasting indicate some low levels of internal friction and/or cohesion. Our shape model indicates that, similar to other top-shaped asteroids, Bennu formed by reaccumulation and underwent past periods of fast spin, which led to its current shape. Today, Bennu might follow a different evolutionary pathway, with an interior stiffness that permits surface cracking and mass wasting.

Prior to the arrival of the OSIRIS-REx (Origins, Spectral Interpretation, Resource Identification, and Security-Regolith Explorer) spacecraft, radar and lightcurve modelling¹ suggested that Bennu has a 'spinning-top' shape with an equatorial ridge. The mean diameter and the volume were estimated to be 492 ± 20 m and 0.062 ± 0.006 km³, respectively. A single boulder, estimated to be 10–20 m wide, was apparent on a surface that was otherwise smooth at the radar resolution of 7.5 m. A rotation period of 4.297 ± 0.002 h was measured about an axis with a pole at $(87^\circ, -65^\circ) \pm 4^\circ$ in J2000 equatorial coordinates².

Here we reassess the shape of Bennu using images collected by the OSIRIS-REx Camera Suite (OCAMS³). We developed a global digital terrain model (GDTM) of the asteroid (Fig. 1) as the basis for geophysical investigations. The measured GDTM parameters are given in Table 1. We generated the GDTM using stereophotoclinometry (SPC⁴), a well-established technique that merges stereo imaging with photoclinometry. An assessment that includes data from the OSIRIS-REx Laser Altimeter (OLA⁵) collected in December 2018 (Fig. 1) independently quantifies uncertainties in the GDTM (Supplementary Fig. 1).

The GDTM's best-fit ellipsoid is given by $(252.78 \pm 0.05) \times (246.2 \pm 0.09) \times (228.69 \pm 0.12)$ m. Its average diameter is 490.06 ± 0.16 m, consistent with the diameter previously determined from radar. The

GDTM has a volume of 0.0615 ± 0.0001 km³—also similar to the pre-encounter value—and a surface area of 0.782 ± 0.004 km². We evaluate a new pole position of $(85.65 \pm 0.12, -60.17 \pm 0.09)^\circ$. The SPC-derived rotation period is similar to the pre-encounter estimate and statistically indistinguishable from the value of 4.276057 ± 0.000002 h determined using lightcurves from Earth-based and OSIRIS-REx Approach-phase imaging^{6,7}. The prime meridian is defined by a dark patch on a distinct boulder in Bennu's southern (–Z) hemisphere (Supplementary Fig. 2). A small (<2 m) centre-of-mass/centre-of-figure offset is present, dominantly in the direction of the prime meridian.

Bennu's volume is 3.5 times that of Itokawa⁸ and one-sixth that of (162173) Ryugu⁹, two other small (<1 km diameter) rubble-pile asteroids. The OSIRIS-REx mass estimate for Bennu is $7.329 \pm 0.009 \times 10^{10}$ kg (ref. 10). Using the physical properties of the carbonaceous Ivuma (CI) and Mighei (CM) meteorites, to which Bennu is compositionally linked^{7,11}, along with the mass and volume of Bennu, we estimate the asteroid's density to be $1,190 \pm 13$ kg m⁻³. Given the average measured bulk densities of CI and CM meteorites ($1,570$ – $2,200$ kg m⁻³ (ref. 12)), the macroporosity (or bulk porosity) of Bennu ranges from 25% (CI) to 50% (CM). Considering the substantial microporosity displayed in CI and CM chondrites, the corresponding total porosity of Bennu is 50–60%—similar to that of other carbonaceous (C)-group asteroids¹³.

¹The Johns Hopkins University Applied Physics Laboratory, Laurel, MD, USA. ²The Centre for Research in Earth and Space Science, York University, Toronto, Ontario, Canada. ³Planetary Science Institute, Tucson, AZ, USA. ⁴Department of Earth, Ocean and Atmospheric Sciences, University of British Columbia, Vancouver, British Columbia, Canada. ⁵Lockheed Martin Space, Littleton, CO, USA. ⁶NASA Goddard Space Flight Center, Greenbelt, MD, USA. ⁷Lunar and Planetary Laboratory, University of Arizona, Tucson, AZ, USA. ⁸KinetX Aerospace, Inc., Simi Valley, CA, USA. ⁹Smithsonian Institution National Museum of Natural History, Washington, DC, USA. ¹⁰Southwest Research Institute, Boulder, CO, USA. ¹¹Université Côte d'Azur, Observatoire de la Côte d'Azur, CNRS, Laboratoire Lagrange, Nice, France. ¹²Smead Department of Aerospace Engineering, University of Colorado, Boulder, CO, USA. ¹³University of Tokyo, Tokyo, Japan. ¹⁴Aizu University, Aizu-Wakamatsu, Japan. ¹⁵Kobe University, Kobe, Japan. ¹⁶Nagoya University, Nagoya, Japan. ¹⁷JAXA Institute of Space and Astronautical Science, Sagami-hara, Japan. ¹⁸A list of participants and their affiliations appears in the online version of the paper. *e-mail: olivier.barnouin@jhuapl.edu

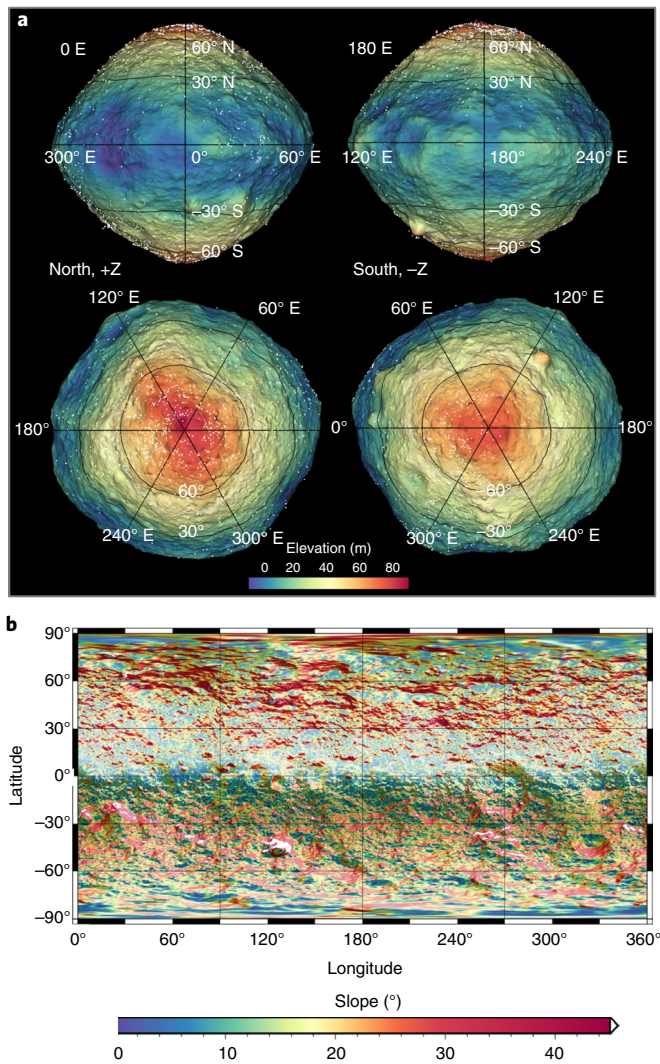


Fig. 1 | The GDTM of Bennu. **a**, Several views of the GDTM, colored by elevation. **b**, A shaded relief of the GDTM with slopes. The poles of Bennu are high, and the equator is a low-lying region. OLA footprint locations are overlain (white spots). The GDTM has a resolution of ~ 0.8 m per facet and a total of 1.5 million facets. The textured appearance in many regions of the GDTM is not noise, but evidence for metre-scale boulders that influence the roughness of the model.

Global shape attributes

The OSIRIS-REx observations confirm key aspects of the Earth-based radar shape model¹. By fitting a low-degree spherical harmonic expansion (essentially, a series of sines and cosines) to Bennu's GDTM, the top shape, with an equatorial ridge, is seen as strong zonal (latitudinal) degree-2 and degree-4 terms (Fig. 2). In contrast to Ryugu⁹—the other top-shaped asteroid visited by a spacecraft—Bennu's equatorial ridge is muted, and appears diamond-shaped when viewed from the poles (Fig. 3).

The spherical harmonic assessment of Bennu also shows that it has a substantial contribution from the degree-4 sectoral (longitudinal) term (Fig. 2) that is not seen in a similar spherical harmonic analysis of top-shaped Ryugu (methods). In Bennu's case, this term results from at least four major north–south longitudinal ridges observed in the northern (+Z) hemisphere, two of which continue into the southern hemisphere (Figs. 1 and 2). The ridges contribute a root-mean-square amplitude of 8–10 m in the degree-4 sectoral shape (Fig. 2), and the relief from the tops of the ridges to the base of the

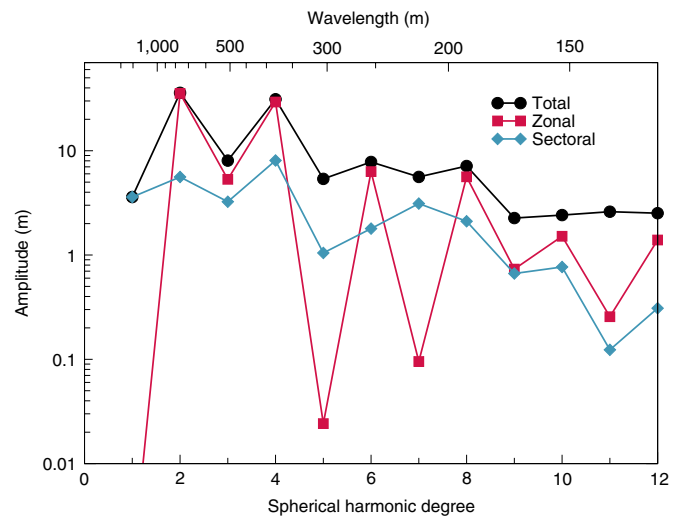


Fig. 2 | Amplitude spectrum of a spherical harmonic expansion for the GDTM. Black circles indicate the total amplitude at each spherical harmonics degree. Zonal terms (red) describe contributions to the shape that vary only with latitude; sectoral contributions (blue) vary only with longitude. The large zonal degree-2 and degree-4 terms are a consequence of Bennu's top shape and equatorial ridge. The relatively low amplitudes of the degree-3 and degree-5 terms demonstrate that there is no substantial north–south asymmetry. The degree-4 sectoral terms capture the $\sim 90^\circ$ longitudinal variations in Bennu's shape, which results from the major north–south ridges, that have a root-mean-square globally averaged amplitude of 8–10 m.

low-lying topography between the ridges can be up to 25 m (Fig. 3), with ridge lengths extending from 400 to 780 m. These longitudinal ridges, together with several large candidate craters (defined in Walsh et al.¹⁴), contribute to Bennu's diamond-shaped equatorial profile (Fig. 3). The equatorial signature of these ridges is approximately periodic in longitude with a wavelength of 90° , and accounts for $\sim 33\%$ of the amplitude of the deviations from a circular shape.

Regional surface features

An understanding of the geological evolution of Bennu's shape is facilitated by maps (Fig. 1) of the surface elevation and slope (for example, Cheng et al.¹⁵ and Barnouin-Jha¹⁶). Surface elevation, also known as geopotential altitude¹⁷, is computed as the difference between the gravitational surface potential and a reference potential divided by the magnitude of the local gravitational acceleration g , considering the asteroid mass and spin rate. The slope is computed as the angle between the surface normal and the g vector. Both elevation and slope indicate the direction in which loose surface material may move across the surface. In Bennu's case, the elevation and slopes are highest near the poles and lowest at the equatorial ridge (Fig. 1). The previously described longitudinal ridges are typically high standing relative to their local surroundings and create a distinct feature in the hypsometry distributions of surface elevation (Supplementary Fig. 3).

In addition to the equatorial and longitudinal ridges, other surface features contribute to Bennu's shape (Fig. 4). These include large boulders, craters, mass-wasting deposits and linear features.

The three largest boulders are located in the southern hemisphere (Fig. 4a). The tallest (45° S, 129° E) measures 27 ± 2 m in height and 57×40 m in diameter. The prime meridian boulder (25° S, 0° E) and the largest partially exposed boulder (23° S, 23° E) measure 12 ± 1 m and 13 ± 2 m in height and 34 ± 5 m and 78 ± 12 m in diameter, respectively. These boulders are roughly similar in size to the largest boulder identified on

Table 1 | The physical parameters of Bennu

Parameter	Value
Average radius	244 ± 0.09 m
Best-fit ellipsoid (semi-major axis)	$(252.78 \pm 0.05) \times (246.20 \pm 0.09) \times (228.69 \pm 0.12)$ m
Volume	0.0615 ± 0.0001 km ³
Surface area	0.782 ± 0.004 km ²
Bulk density	$1,190 \pm 13$ kg m ⁻³
Pole	RA = $(85.65 \pm 0.12)^\circ$; dec = $(-60.17 \pm .09)^\circ$
Period (equatorial J2000)	4.276057 ± 0.000002 h
Period rate of change	$-1.02 + / - 0.15$ seconds per century
Centre of mass/centre of figure offset ^a	$(1.38 \pm 0.04, -0.43 \pm 0.07, -0.12 \pm 0.27)$ m
Gravitational acceleration ^a	Weighted mean = 0.0000595 ± 0.0000001 m s ⁻² Median = 0.0000615 m s ⁻²
Slopes ^a	0.0° to 92.0° , weighted mean = $17 \pm 2^\circ$ Median = 16.3°

The average radius (diameter in text) is computed using an equivalent volume sphere. dec = declination; RA = right ascension. ^aAssumes uniform density.

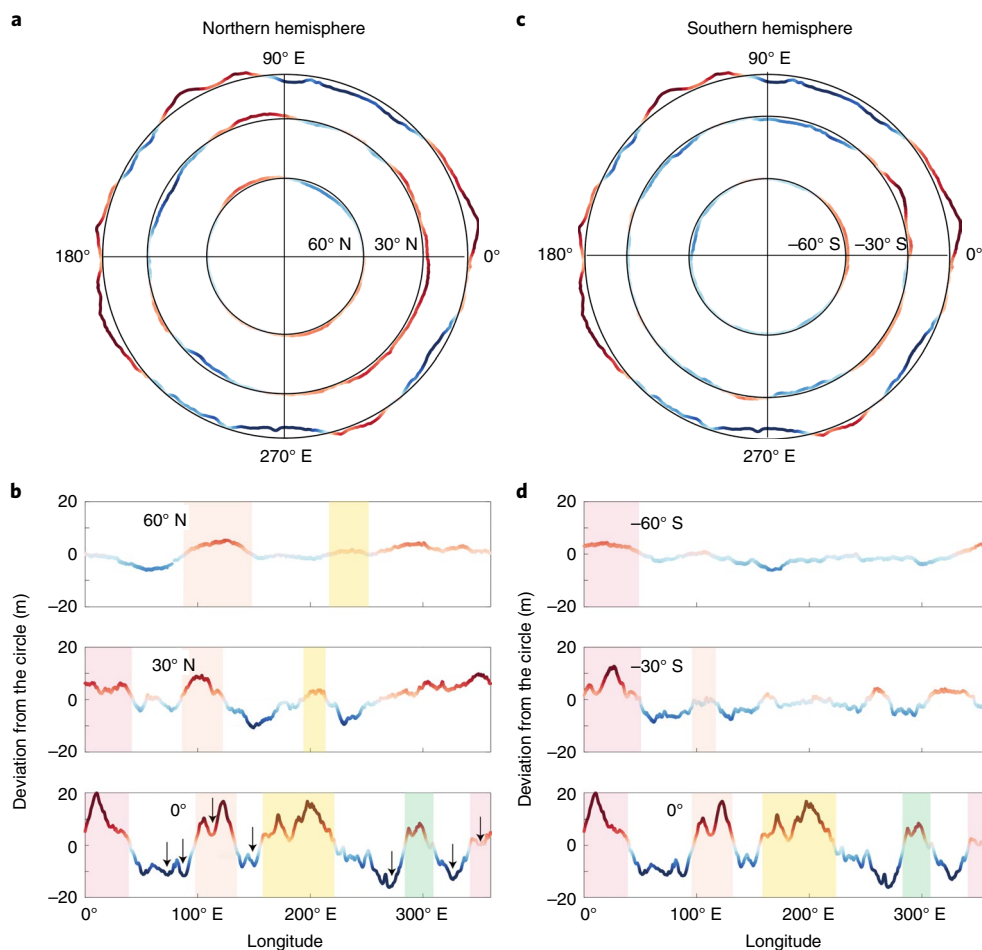


Fig. 3 | Deviations of Bennu's radius from that of a circle, for different latitudinal cross-sections. a, Best-fit circles for the circumference of Bennu at 0°, 30° N and 60° N overlap on radius measurements of Bennu's shape cross-sections and colour coded by deviations from the circle. **b**, Deviations from the circular shape for 0°, 30° N and 60° N. The shaded regions represent consistently elevated topography above the best-fit circles, interpreted as roughly longitudinally oriented ridges. At least two of the ridges extend from the north to the south high-latitude regions. Arrows indicate locations of candidate craters¹⁴ that have short wavelength contributions to the equatorial shape. **c,d**, Similar plots for the southern hemisphere.

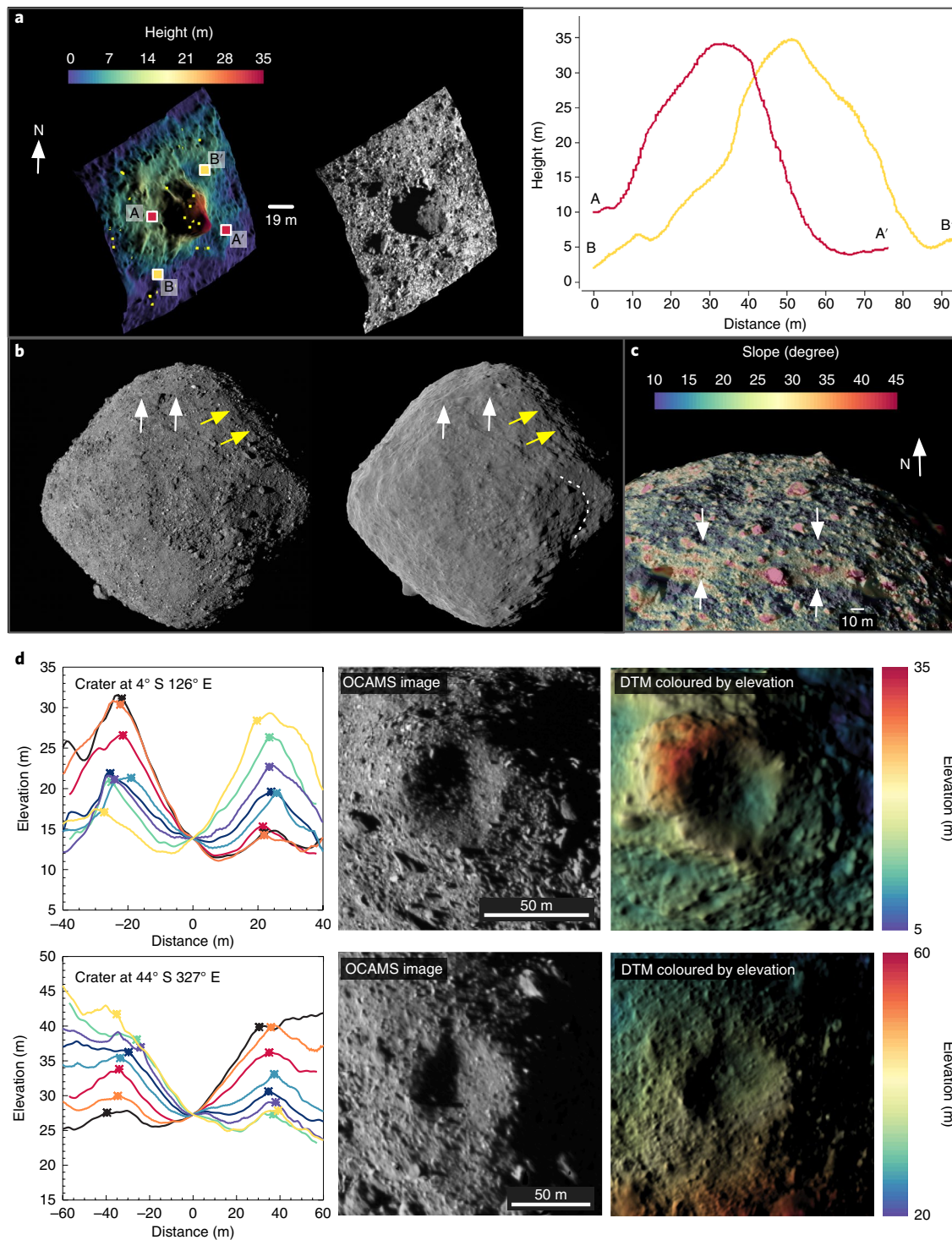


Fig. 4 | DTMs and images of geological features that contribute to the shape of Bennu. a, Large boulders (for example, 45° S, 132° E) influence the global attributes of the GDTM. **b–d**, Additional contributors to the shape include long grooves (**b**, yellow arrows), scarps (**b** and **c**, white arrows), mass wasting (dashed line on the GDTM in **b**; more details given in Walsh et al.¹⁴) and craters (**d**). The local DTM of the boulder in **a** (left) has a 1.12 m root mean squared (r.m.s.) error derived from the OLA returns, shown as yellow dots in the left panel. The bottom crater in **d** has overlapping OLA returns, and the r.m.s. difference between the OLA points and the local DTM is 45 cm. The d/D of the top and bottom craters in **d** are 0.24 ± 0.03 and 0.14 ± 0.02 , respectively, with respect to elevation. The crater profile colours indicate orientations (orange, E–W; green, N–S; navy blue, SW–NE; yellow, SSE–NNW; purple, SSW–NNE; black, NE–SW; blue, SEE–NWW; orange, NEE–SWW). More information is given in Methods.

Itokawa (20 ± 1 m high and 46 m long)¹⁸. There is also a large population of small boulders with heights near 1–3 m; these contribute to the mottled appearance of the GDTM (Fig. 1a). The

largest boulder is superimposed on one of the southern longitudinal ridges, and might be an outcrop of a structural unit that forms the ridge.

We measured the diameter (D) and depth (d) of several candidate impact craters (Fig. 4¹⁴), the largest of which (6°S, 270°E) has a $D=157\pm 11$ m. A strictly geometric assessment of four of these craters with D from 46 to 69 m gives an average $d/D\approx 0.13\pm 0.04$; when measured relative to elevation (as on planets), the average d/D is $\sim 0.16\pm 0.06$. The morphometry of these craters is similar to those of impact craters on other, larger asteroids ((433) Eros, (21) Lutetia and (4) Vesta), for which the geometric $d/D\approx 0.15$ (ref. ¹⁹), and to (253) Mathilde, a large C-type asteroid with an inferred composition similar to that of Bennu, for which the geometric d/D ranges from 0.12 to 0.25 (ref. ²⁰). As on these other asteroids, Bennu's candidate craters possess raised rims, which indicates they are probably the product of impacts. The craters on Bennu are deeper than those on Itokawa, where the maximum geometric d/D is 0.1 (ref. ²¹).

Linear features such as grooves and scarps, cross-cut the surface of Bennu (Fig. 4). They have several orientations. One of the longest grooves (Fig. 4c) extends from the pole to the equator; it is 10–15 m wide and has a depth of 3 ± 1 m. Other grooves have similar aspect ratios, trend east to west or have slightly northeast–southwest orientations and span lengths of many tens to hundreds of metres. The most pronounced long scarp is located in the northern hemisphere (Fig. 4b,c), spanning at least 120° of longitude at $\sim 50^\circ$ N. It drops down by 3–6 m with a 40° slope.

The GDTM shows evidence of areas where mass wasting has occurred. The best example is a material flow that infills the largest candidate crater on Bennu (Fig. 4b; Walsh et al.¹⁴ gives details); it covers over the western rim and leaves a deposit ~ 5 m in thickness that post-dates the crater. Boulder concentrations at the bases of long slopes¹⁴, particularly between the high-standing ridges (Supplementary Fig. 4), provide further evidence of widespread mass wasting.

Inferences on the present and past interior structure of Bennu

Several aspects of Bennu's topography support the pre-encounter assessment¹ that Bennu is a rubble-pile asteroid. At 50–60%, Bennu's high total porosity is incompatible with a monolithic body and may be the strongest evidence for a rubble-pile interior. A companion paper¹⁰ models the density inhomogeneities in terms of a few large boulders, consistent with a rubble-pile structure, and thereby explains Bennu's centre-of-mass/centre-of-figure offset and spin-axis orientation in the body frame. In addition, Bennu's largest boulders are too large to be ejecta^{14,22} from the largest crater candidates and, therefore, are probably remnants of Bennu's parent body accreted after its disruption²³.

Nevertheless, Bennu's shape and surface features imply that the asteroid has some structural rigidity, despite being a rubble pile. Evidence for structural strength includes Bennu's non-hydrostatic shape, the high-standing longitudinal ridges, the long linear grooves, and apparent mass wasting. A fluid-like hydrostatic shape (for example, a Maclaurin ellipsoid²⁴) with Bennu's density and rotation rate is not stable. Assuming, as a limiting case, that Bennu is composed of granular material with no cohesion, it must have a minimum internal friction angle of at least 18° to support the current shape (Supplementary Fig. 5). This friction angle—which in the absence of cohesion can, by Coulomb's law, equal the angle of repose for a granular material (for example, Iverson et al.²⁵)—is similar to the global average surface slope of $17\pm 2^\circ$ (ref. ¹⁰). The longitudinal ridges denote internal stiffness because they support material above the surrounding terrain. Long linear grooves are seen on other asteroids and are considered evidence for structural coherence²⁶. Such grooves are expressions of cracks, which cannot propagate to become long linear structures in asteroids that lack structural integrity¹⁹. Finally, several models for the rotational evolution of asteroids show that those with stiffer interiors (resulting from packing of internal constituents, for example) are more likely to generate a mass wasting similar to that observed on Bennu^{27–29}.

Bennu may not have always been so rigid. The large number of crater candidates at low latitudes¹⁴ near the equatorial ridge ($<30^\circ$) indicate that the ridge is old. If the ridge formed by re-accumulation after the disruption of Bennu's parent body, as some models propose^{30,31}, then the past interior strength could be similar to that of today. However, if the radiative-driven spin-up processes known collectively as the YORP (Yarkovsky–O'Keefe–Radzievskii–Paddack) effect³² drove its formation¹, then current models^{28,29,33} indicate that the equatorial ridge is most probably the product of a more compliant interior and surface material, which more easily deformed to build up the ridge. In the latter case, Bennu would have been weaker at some point in its past.

How, though, are the high-standing longitudinal ridges formed? Numerical investigations of the disruption of rubble piles due to spin-up^{34,35} show that when a ~ 1 –30 Pa cohesion is present, the asteroid fails in well-defined and fairly evenly spaced longitudinal wedges. Such wedges could be manifested as longitudinal ridges. The minimum internal cohesive strength of Bennu is estimated to be 1 Pa (ref. ¹⁰). Hence, these high-standing longitudinal ridges may indicate that Bennu may have been close to fully disrupting during the equatorial ridge formation.

Some of the characteristics of Bennu's shape and surface geology differ from those of other small, rubble-pile asteroids visited by spacecraft. Itokawa, a siliceous-type rubble-pile asteroid, shows little change in its overall shape over time, lacks grooves and troughs, and its surface processes are limited to near-surface ones driven by cratering and thermal fragmentation for example, Mazrouei et al.¹⁸, Marci et al.¹⁹, Miyamoto et al.³⁶ and Delbo et al.³⁷). Ryugu, which is a C-group rubble-pile asteroid similar to Bennu, presents different surface characteristics and a slightly different shape to that of Bennu, with less-apparent evidence for interior rigidity⁷ and fewer obvious surface displacements. Hence, the evolutionary paths of individual asteroids can lead to diverse interior properties, shapes and surface features, even among asteroids that are similar in size or type. There is no one-size-fits-all rubble-pile asteroid.

Online content

Any methods, additional references, Nature Research reporting summaries, source data, statements of data availability and associated accession codes are available at <https://doi.org/10.1038/s41561-019-0330-x>.

Received: 30 January 2019; Accepted: 15 February 2019;
Published online: 19 March 2019

References

- Nolan, M. et al. Shape model and surface properties of the OSIRIS-REx target asteroid (101955) Bennu from radar and lightcurve observations. *Icarus* **226**, 629–640 (2013).
- Hergenrother, C. W. et al. Lightcurve, color and phase function photometry of the OSIRIS-REx target asteroid (101955) Bennu. *Icarus* **226**, 663–670 (2013).
- Rizk, B. et al. OCAMS: the OSIRIS-REx Camera Suite. *Space Sci. Rev.* **214**, 26 (2018).
- Gaskell, R. W. et al. Characterizing and navigating small bodies with imaging data. *Meteorit. Planet. Sci.* **43**, 1049–1061 (2008).
- Daly, M. G. et al. The OSIRIS-REx Laser Altimeter (OLA) investigation and instrument. *Space Sci. Rev.* **198**, 1–26 (2017).
- Hergenrother, C. W. et al. Operational environment and rotational acceleration of asteroid (101955) Bennu from OSIRIS-REx observations. *Nat. Commun.* <https://doi.org/10.1038/s41467-019-09213-x> (2019).
- Lauretta, D. S. et al. The unexpected surface of asteroid (101955) Bennu. *Nature* <https://doi.org/10.1038/s41586-019-1033-6> (2019).
- Abe, S. et al. Mass and local topography measurements of Itokawa by Hayabusa. *Science* **312**, 1344–1347 (2006).
- Watanabe, S. et al. Hayabusa2 arrives at the carbonaceous asteroid 162173 Ryugu — a spinning-top-shaped rubble pile. *Science* <https://doi.org/10.1126/science.aav8032> (in the press).
- Scheeres, D. J. et al. The dynamic geophysical environment of (101955) Bennu based on OSIRIS-REx measurements. *Nat. Astron.* <https://doi.org/10.1038/s41550-019-0721-3> (2019).

11. Hamilton, V. E. et al. Evidence for widespread hydrated minerals on asteroid (101955) Benu. *Nat. Astron.* <https://doi.org/10.1038/s41550-019-0722-2> (2019).
12. Macke, R. J., Consolmagno, G. J. & Britt, D. T. Density, porosity, and magnetic susceptibility of carbonaceous chondrites. *Meteorit. Planet. Sci.* **46**, 1842–1862 (2011).
13. Scheeres, D. J., Britt, D., Carry, D. & Holsapple, K. A. in *Asteroids IV* (eds Michel, P., DeMeo, F. E. & Bottke, W. F.) 745–766 (University of Arizona Press, Tucson, 2015).
14. Walsh, K. J. et al. Craters, boulders and regolith of (101955) Benu indicative of an old and dynamic surface. *Nat. Geosci.* <https://doi.org/10.1038/s41561-019-0326-6> (2019).
15. Cheng, A. F. et al. Small-scale topography of 433 Eros from laser altimetry and imaging. *Icarus* **155**, 51–74 (2002).
16. Barnouin-Jha, O. S. et al. Small-scale topography of 25143 Itokawa from the Hayabusa laser altimeter. *Icarus* **198**, 108–124 (2008).
17. Scheeres, D. J. et al. The geophysical environment of Benu. *Icarus* **276**, 116–140 (2016).
18. Mazrouei, S., Daly, M. G., Barnouin, O. S., Ernst, C. M. & DeSouza, I. Block distributions on Itokawa. *Icarus* **229**, 181–189 (2014).
19. Marchi, S., Chapman, C. R., Barnouin, O. S., Richardson, J. E., Vincent, J.-B. in *Asteroids IV* (eds Michel, P., DeMeo, F. E. & Bottke, W. F.) 725–744 (University of Arizona Press, Tucson, 2015).
20. Thomas, P. C. et al. Mathilde: size, shape, and geology. *Icarus* **140**, 17–27 (1999).
21. Hirata, N. et al. A survey of possible impact structures on 25143 Itokawa. *Icarus* **200**, 486–502 (2009).
22. Bart, G. D. & Melosh, H. J. Using lunar boulders to distinguish primary from distant secondary impact craters. *Geophys. Res. Lett.* **34**, L07203 (2007).
23. Michel, P. & Richardson, D. C. Collision and gravitational reaccumulation: possible formation mechanism of the asteroid Itokawa. *Astron. Astrophys.* **554**, 1–4 (2013).
24. Holsapple, K. A. Equilibrium figures of spinning bodies with self-gravity. *Icarus* **172**, 272–303 (2004).
25. Iverson, R. M. The physics of debris flows. *Rev. Geophys.* **35**, 245–296 (1997).
26. Prockter, L. et al. Surface expressions of structural features on Eros. *Icarus* **155**, 75–93 (2002).
27. Walsh, K. J., Richardson, D. C. & Michel, P. Rotational breakup as the origin of small binary asteroids. *Nature* **454**, 188–191 (2008).
28. Hirabayashi, M., Sanchez, P. & Scheeres, D. J. Internal structure of asteroids having surface shedding due to rotational instability. *Astrophys. J.* **808**, 63 (2015).
29. Zhang, Y. et al. Creep stability of the proposed AIDA mission target 65803 Didymos: I. Discrete cohesionless granular physics model. *Icarus* **294**, 98–123 (2017).
30. Barnouin, O. S., Michel, P. & Richardson, D. C. A preliminary assessment of asteroid shapes produced by impact disruption and re-creation: application to the AIDA target. *Geophys. Res. Abstracts* **18**, 17584 (2016).
31. Michel, P. et al. Disruption and reaccumulation as the possible origins of Ryugu and Benu top shapes. In *Lunar Planetary Sci. Conf.* 50 abstr. 1659 (2019).
32. Rubincam, D. P. Radiative spin-up and spin-down of small asteroids. *Icarus* **148**, 2–11 (2000).
33. Hirabayashi, M. & Scheeres, D. J. Stress and failure analysis of rapidly rotating asteroid (29075) 1950 DA. *Astrophys. J. Lett.* **798**, L8 (2014).
34. Sanchez, P. & Scheeres, D. J. Disruption patterns of rotating self-gravitating aggregates: a survey on angle of friction and tensile strength. *Icarus* **271**, 453–471 (2016).
35. Zhang, Y. et al. Rotational failure of rubble-pile bodies: influences of shear and cohesive strengths. *Astrophys. J.* **857**, 15 (2018).
36. Miyamoto, H. et al. Regolith migration and sorting on asteroid Itokawa. *Science* **316**, 1011 (2007).
37. Delbo, M. et al. Thermal fatigue as the origin of regolith on small asteroids. *Nature* **508**, 233–236 (2014).

Acknowledgements

This material is based on work supported by NASA under contract NNM10AA11C issued through the New Frontiers Program. The Canadian team members were supported by the Canadian Space Agency. P.M. acknowledges funding support from the French space agency CNES and from Academies of Excellence: Complex systems and Space, environment, risk, and resilience, part of the IDEX JEDI of the Université Côte d'Azur.

Author contributions

O.S.B. is the OSIRIS-REx Altimetry Working Group (AltWG) lead responsible for the generation of all the global and local digital terrain models produced during the OSIRIS-REx Mission. He worked with M.G.D., the instrument Principle Investigator for OLA, as well as E.E.P., R.W.G. and J.R.W., who developed and tested the SPC software, and subsequently made the GDTM. C.L.J. and M.M.A. undertook verification of the SPC GDTM and assessed the circularity of Benu's circumference, and J.H.R. and G.A.N. performed the spherical harmonic and Maclaurin assessment of the shape. M.E.P., as the AltWG system engineer, facilitated verification of the GDTM products and contributed to lineament assessments. H.C.M.S. provided roughness assessments of Benu. R.T.D. measured crater shapes under the guidance of E.E.B. R.T.D. also performed the hypsometry analysis. J.A.S. is the OLA instrument scientist and helped to verify the SPC products. R.M.E., A.H.N., L.N. and C.M.E. helped to generate the final topographic products (for example, elevation, slope and radius) used in the analyses presented. C.M.E. also aided R.T.D. in the crater analysis. W.V.B. and M.C.N. oversaw the collection of the data necessary to make the presented GDTM. C.D.A., M.C.M. and E.M.M. are part of the OSIRIS-REx flight dynamics team who worked closely with the AltWG and provided an independent verification of the SPC model presented. B.R. and C.D.D. are the lead engineers for OCAMS, without which the SPC shape models would not be possible. E.R.J., K.J.W., P.M., S.R.S., R.-L.B. and E.M.M. are members of the OSIRIS-REx Regolith Working Group who either mapped, modelled, or undertook analyses that are part of the presented manuscript. D.J.S. and J.M. worked with the OSIRIS-REx flight dynamics team to generate the asteroid mass needed for the porosity discussion and provided some of the shape inferences from their modelling efforts. S.S., N.H. and S.W. are Hayabusa2 team members who provided access to Ryugu data that was used to motivate some of the discussion presented in this study. K.N.B., D.N.D. and C.A.B. provided the boulder distribution used to demonstrate the influence of the longitudinal ridges on boulder locations. D.S.L. is the OSIRIS-REx Principal Investigator. O.S.B., M.G.D., C.L.J. and M.E.P. drafted the manuscript, which was reviewed by all the authors. The entire OSIRIS-REx Team made the Benu encounter possible.

Competing interests

The authors declare no competing interests.

Additional information

Supplementary information is available for this paper at <https://doi.org/10.1038/s41561-019-0330-x>.

Reprints and permissions information is available at www.nature.com/reprints.

Correspondence and requests for materials should be addressed to O.S.B.

Publisher's note: Springer Nature remains neutral with regard to jurisdictional claims in published maps and institutional affiliations.

© The Author(s), under exclusive licence to Springer Nature Limited 2019

Methods

Uncertainty of the Benu shape model. Supplementary Fig. 1 gives a description of how we estimated the uncertainty of Benu's GDTM. This model, v20, was developed from an imaging campaign specifically designed to generate it, which started at the beginning of November 2018 and ended on 17 January 2019. All our extensive testing³⁷ shows that we achieved a GDTM with accuracies near the ground-sample distance of the imaging input into the model. The ground-sample distances of the images employed in this model vary from 0.3 to 2 m, with most images near 0.5–0.6 m. Over 1,500 images were used to make these models. The observations were designed specifically to ensure that SPC could produce the best product as rapidly as possible. This was achieved by ensuring that each region on Benu's surface was imaged with a ground-sample distance of ~0.5 m from at least four directions (north, south, east and west) with separation angles near 90°, and one image near a zero degrees phase angle for the albedo.

Definition of the prime meridian. Supplementary Fig. 2 gives a description of the location of the prime meridian determined on Benu.

Hypsometry distributions. Supplementary Fig. 3 for comparisons of Benu's hypsometry distribution³⁸ with other asteroids such as Eros³⁹ and Itokawa⁴⁰. Hypsometry is a measurement of the distribution of surface elevations.

Spherical harmonic solution of Benu and Ryugu. In this study, we used an orthonormalized versions of the spherical harmonics, where:

$$Y_{\ell}^m(\theta, \phi) = \sqrt{\frac{2\ell + 1}{4\pi} \frac{(\ell - m)!}{(\ell + m)!}} P_{\ell}^m(\cos \theta) e^{im\phi}$$

ℓ and m are the spherical harmonic degree and order respectively, P_{ℓ}^m is the associated Legendre function and θ and ϕ are the co-latitude and longitude, respectively. The results for Benu are shown in Fig. 1.

We undertook a similar spherical harmonic assessment of the shape of Ryugu as that presented here for Benu. The model was kindly provided by the Hayabusa2 team, although we did not receive permission to show a graphical representation of our findings. Nevertheless, we can confirm that the amplitude of the sectoral terms at degree-2 and degree-4 for Ryugu are considerably smaller than those seen for the spherical harmonic assessment of Benu. A similar assessment of the KW4 radar model also shows small sectoral terms. Benu thus has distinctive topographic features, expressed by the longitudinal ridges described in this paper, that are not seen on other top-shaped asteroids.

Boulder distributions between north–south ridges. The longitudinal ridges influence the distribution of boulders⁴¹ at mid-to-low latitudes, as seen in Supplementary Fig. 4.

Maclaurin spheroid. The Maclaurin spheroid is the simplest model for a rotating ellipsoidal in equilibrium. The Maclaurin spheroid is an oblate spheroid that arises when a fluid, self-gravitating body of uniform density ρ (a reasonable assumption for a small, rubble-pile asteroid) rotates with constant angular velocity. The Maclaurin spheroid model can be generalized to cohesionless solids²⁴. The scaled spin is defined by:

$$\frac{\Omega^2}{\pi G \rho} = \frac{2\alpha \sqrt{m + 2\alpha^2}}{m(1 - \alpha^2)^{3/2}} \cos^{-1} \alpha - \frac{2(m + 2)\alpha^2}{m(1 - \alpha^2)}$$

where G is the gravitational constant, Ω is the asteroid spin rate, α is the ratio of the polar (c) and equatorial (a) axes and φ is the angle of internal friction. A strengthless (that is, fluid) body with no internal friction would have $m = 1$, the Maclaurin formula. We show a range of figures as a function of m in Supplementary Fig. 5. Alternative figures of equilibria exist. Jacobi ellipsoids, for example, admit triaxial solutions^{24,42}, although the distinction is unlikely to be significant for Benu, and is more relevant to prolate asteroids (for example, Eros or Itokawa).

Expanded caption for Fig. 4. The OCAMS image in Fig. 4a was collected on 16 December 2018 at 19:45:27 coordinated universal time (UTC). Note that SPC tends to broaden the aprons of high-standing features, especially when there is rapidly changing topography, so the match between the image in the middle and the local DTM is not perfect, but still fairly good. The left OCAMS image in Fig. 4b was obtained on 13 December 2018 at 01:01:48 UTC. The steep slopes (red) in Fig. 4c (OCAMS image collected 2 December 2018 at 07:12:28 UTC) highlight the scarp shown by the white arrows in Fig. 4b. The dashed lines in Fig. 4b show evidence for a mass wasting deposit that flowed from a high point in the west into the large crater candidate (more details given in Walsh et al.¹⁴). Each row in Fig. 4d shows eight elevation profiles through the centre of a corresponding candidate crater (location indicated in Fig. 4d). The images are excerpted from OCAMS data collected on 12 December 2018 at 04:44:20 UTC (top row in Fig. 4d) and 2 December 2018 at 08:59:47 UTC (bottom row in Fig. 4d) and were draped on the highest-resolution Benu shape model (v20 (Methods)). The viewing geometry is approximately normal to the crater planform. The local DTMs centred on each crater are coloured by elevation and have a 50 cm ground-sample distance. Note that r.m.s. differences between OLA and the DTMs derived from SPC are much smaller than the uncertainty associated with the measurement of boulder heights and crater depths due to regional differences in the topography.

Comparison with earlier versions of the shape model of Benu. Several of the companion OSIRIS-REX manuscripts^{10,11,14,41} used versions v13 or v14 of the Benu GDTM, produced in late December 2018, a month earlier than the version presented here (v20). Supplementary Fig. 6 shows some of the differences between the earlier and later models, and illustrates that the differences are minor and would not affect the conclusions of the companion papers.

Code availability

Most of the image and digital terrain analyses shown were undertaken with the JHUAPL Small Body Mapping Tool (SBMT). It is available for the analysis of a broad suite of asteroid and comet data at sbmt.jhuapl.edu. On release of the OSIRIS-REX data by the PDS, a version of SBMT with those data will be made publicly available. The spherical harmonic assessment was performed using the Spherical Harmonic Transform Library hosted at Mathworks (<https://www.mathworks.com/matlabcentral/fileexchange/43856-real-complex-spherical-harmonic-transform-gaunt-coefficients-and-rotations>). The SPC code used to develop the GDTM of Benu can be made available with special permission. Please contact the corresponding author for additional information on how.

Data availability

Raw through to calibrated data sets will be available via the Planetary Data System (PDS) (<https://sbn.psi.edu/pds/resource/orex/>). Data are delivered to the PDS according to the OSIRIS-REX Data Management Plan available in the OSIRIS-REX PDS archive. Higher-level products (for example, the GDTM) discussed here will be available in the PDS one year after departure from the asteroid.

References

- Barnouin, O. S. et al. Altimetry efforts at Benu. In *Lunar Planetary Sci. Conf. 49* abstr. 1041 (2018).
- Gaskell, R. W. *Gaskell Eros Shape Model V1.0. NEAR-A-MSI-5-EROSHAPE-V1.0. NASA Planetary Data System* (NASA, 2008).
- Gaskell, R. W. et al. *Itokawa Shape Model V1.0. HAY-A-AMICA-5-ITOKAWASHAPE-V1.0. NASA Planetary Data System* (NASA, 2008).
- DellaGiustina, D. N. et al. Properties of rubble-pile asteroid (101955) Benu from OSIRIS-REX imaging and thermal analysis. *Nat. Astron.* <https://doi.org/10.1038/s41550-019-0731-1> (2019).
- Richardson, J. E. & Bowling, T. J. Investigating the combined effects of shape, density, and rotation on small body surface slopes and erosion rates. *Icarus* **234**, 53–65 (2014).

The OSIRIS-REx Team

D. E. Highsmith¹⁹, J. Small¹⁹, D. Vokrouhlický²⁰, N. E. Bowles²¹, E. Brown²¹, K. L. Donaldson Hanna²¹, T. Warren²¹, C. Brunet²², R. A. Chicoine²², S. Desjardins²², D. Gaudreau²², T. Haltigin²², S. Millington-Veloza²², A. Rubi²², J. Aponte²³, N. Gorius²³, A. Lunsford²³, B. Allen²⁴, J. Grindlay²⁴, D. Guevel²⁴, D. Hoak²⁴, J. Hong²⁴, D. L. Schrader²⁵, J. Bayron²⁶, O. Golubov²⁷, P. Sánchez²⁷, J. Stromberg²⁸, M. Hirabayashi²⁹, C. M. Hartzell³⁰, S. Oliver³¹, M. Rascon³¹, A. Harch³², J. Joseph³², S. Squyres³², D. Richardson³³, J. P. Emery³⁴, L. McGraw³⁴, R. Ghent³⁵, R. P. Binzel³⁶, M. M. Al Asad⁴, C. L. Johnson^{3,4}, L. Philpott⁴, H. C. M. Susorney⁴, E. A. Cloutis³⁷, R. D. Hanna³⁸, H. C. Connolly Jr.³⁹, F. Ciceri⁴⁰, A. R. Hildebrand⁴⁰, E.-M. Ibrahim⁴⁰, L. Breitenfeld⁴¹, T. Glotch⁴¹, A. D. Rogers⁴¹, B. E. Clark⁴², S. Ferrone⁴², C. A. Thomas⁴³, H. Campins⁴⁴, Y. Fernandez⁴⁴, W. Chang⁴⁵, A. Chevront⁴⁶, D. Trang⁴⁷, S. Tachibana⁴⁸, H. Yurimoto⁴⁸, J. R. Brucato⁴⁹, G. Poggiali⁴⁹, M. Pajola⁵⁰, E. Dotto⁵¹, E. Mazzotta Epifani⁵¹, M. K. Crombie⁵², C. Lantz⁵³, M. R. M. Izawa⁵⁴, J. de Leon⁵⁵, J. Licandro⁵⁵, J. L. Rizos Garcia⁵⁵, S. Clemett⁵⁶, K. Thomas-Keprta⁵⁶, S. Van wal¹⁷, M. Yoshikawa¹⁷, J. Bellerose⁵⁷, S. Bhaskaran⁵⁷, C. Boyles⁵⁷, S. R. Chesley⁵⁷, C. M. Elder⁵⁷, D. Farnocchia⁵⁷, A. Harbison⁵⁷, B. Kennedy⁵⁷, A. Knight⁵⁷, N. Martinez-Vlasoff⁵⁷, N. Mastrodemos⁵⁷, T. McElrath⁵⁷, W. Owen⁵⁷, R. Park⁵⁷, B. Rush⁵⁷, L. Swanson⁵⁷, Y. Takahashi⁵⁷, D. Velez⁵⁷, K. Yetter⁵⁷, C. Thayer⁵⁸, C. Adam⁸, P. Antreasian⁸, J. Bauman⁸, C. Bryan⁸, B. Carcich⁸, M. Corvin⁸, J. Geeraert⁸, J. Hoffman⁸, J. M. Leonard⁸, E. Lessac-Chenen⁸, A. Levine⁸, J. McAdams⁸, L. McCarthy⁸, D. Nelson⁸, B. Page⁸, J. Pelgrift⁸, E. Sahr⁸, K. Stakkestad⁸, D. Stanbridge⁸, D. Wibben⁸, B. Williams⁸, K. Williams⁸, P. Wolff⁸, P. Hayne⁵⁹, D. Kubitschek⁵⁹, M. A. Barucci⁶⁰, J. D. P. Deshapriya⁶⁰, S. Fornasier⁶⁰, M. Fulchignoni⁶⁰, P. Hasselmann⁶⁰, F. Merlin⁶⁰, A. Praet⁶⁰, E. B. Bierhaus⁵, O. Billett⁵, A. Boggs⁵, B. Buck⁵, S. Carlson-Kelly⁵, J. Cerna⁵, K. Chaffin⁵, E. Church⁵, M. Coltrin⁵, J. Daly⁵, A. Deguzman⁵, R. Dubisher⁵, D. Eckart⁵, D. Ellis⁵, P. Falkenstern⁵, A. Fisher⁵, M. E. Fisher⁵, P. Fleming⁵, K. Fortney⁵, S. Francis⁵, S. Freund⁵, S. Gonzales⁵, P. Haas⁵, A. Hasten⁵, D. Hauf⁵, A. Hilbert⁵, D. Howell⁵, F. Jaen⁵, N. Jayakody⁵, M. Jenkins⁵, K. Johnson⁵, M. Lefevre⁵, H. Ma⁵, C. Mario⁵, K. Martin⁵, C. May⁵, M. McGee⁵, B. Miller⁵, C. Miller⁵, G. Miller⁵, A. Mirfakhrai⁵, E. Muhle⁵, C. Norman⁵, R. Olds⁵, C. Parish⁵, M. Ryle⁵, M. Schmitzer⁵, P. Sherman⁵, M. Skeen⁵, M. Susak⁵, B. Sutter⁵, Q. Tran⁵, C. Welch⁵, R. Witherspoon⁵, J. Wood⁵, J. Zareski⁵, M. Arvizu-Jakubicki⁷, E. Asphaug⁷, E. Audi⁷, R.-L. Ballouz⁷, R. Bandrowski⁷, K. J. Becker⁷, T. L. Becker⁷, S. Bendall⁷, C. A. Bennett⁷, H. Bloomenthal⁷, D. Blum⁷, W. V. Boynton⁷, J. Brodbeck⁷, K. N. Burke⁷, M. Chojnacki⁷, A. Colpo⁷, J. Contreras⁷, J. Cutts⁷, C. Y. Drouet d'Aubigny⁷, D. Dean⁷, D. N. DellaGiustina⁷, B. Diallo⁷, D. Drinnon⁷, K. Drozd⁷, H. L. Enos⁷, R. Enos⁷, C. Fellows⁷, T. Ferro⁷, M. R. Fisher⁷, G. Fitzgibbon⁷, M. Fitzgibbon⁷, J. Forelli⁷, T. Forrester⁷, I. Galinsky⁷, R. Garcia⁷, A. Gardner⁷, D. R. Golish⁷, N. Habib⁷, D. Hamara⁷, D. Hammond⁷, K. Hanley⁷, K. Harshman⁷, C. W. Hergenrother⁷, K. Herzog⁷, D. Hill⁷, C. Hoekenga⁷, S. Hooven⁷, E. S. Howell⁷, E. Huettner⁷, A. Janakus⁷, J. Jones⁷, T. R. Karet⁷, J. Kidd⁷, K. Kingsbury⁷, S. S. Balram-Knutson⁷, L. Koelbel⁷, J. Kreiner⁷, D. Lambert⁷, D. S. Lauretta⁷, C. Lewin⁷, B. Lovelace⁷, M. Loveridge⁷, M. Lujan⁷, C. K. Maleszewski⁷, R. Malhotra⁷, K. Marchese⁷, E. McDonough⁷, N. Mogk⁷, V. Morrison⁷, E. Morton⁷, R. Munoz⁷, J. Nelson⁷, M. C. Nolan⁷, J. Padilla⁷, R. Pennington⁷, A. Polit⁷, N. Ramos⁷, V. Reddy⁷, M. Riehl⁷, B. Rizk⁷, H. L. Roper⁷, S. Salazar⁷, S. R. Schwartz⁷, S. Selznick⁷, N. Shultz⁷, P. H. Smith⁷, S. Stewart⁷, S. Sutton⁷, T. Swindle⁷, Y. H. Tang⁷, M. Westermann⁷, C. W. V. Wolner⁷, D. Worden⁷, T. Zega⁷, Z. Zeszut⁷, A. Bjurstrom⁶¹, L. Bloomquist⁶¹, C. Dickinson⁶¹, E. Keates⁶¹, J. Liang⁶¹, V. Nifo⁶¹, A. Taylor⁶¹, F. Teti⁶¹, M. Caplinger⁶², H. Bowles⁶³, S. Carter⁶³, S. Dickenshied⁶³, D. Doerres⁶³, T. Fisher⁶³, W. Hagee⁶³, J. Hill⁶³, M. Miner⁶³, D. Noss⁶³, N. Piacentine⁶³, M. Smith⁶³, A. Toland⁶³, P. Wren⁶³, M. Bernacki⁶⁴,

D. Pino Munoz⁶⁴, S.-i. Watanabe^{16,17}, S. A. Sandford⁶⁵, A. Aqueche⁶, B. Ashman⁶, M. Barker⁶, A. Bartels⁶, K. Berry⁶, B. Bos⁶, R. Burns⁶, A. Calloway⁶, R. Carpenter⁶, N. Castro⁶, R. Cosentino⁶, J. Donaldson⁶, J. P. Dworkin⁶, J. Elsila Cook⁶, C. Emr⁶, D. Everett⁶, D. Fennell⁶, K. Fleshman⁶, D. Folta⁶, D. Gallagher⁶, J. Garvin⁶, K. Getzandanner⁶, D. Glavin⁶, S. Hull⁶, K. Hyde⁶, H. Ido⁶, A. Ingegneri⁶, N. Jones⁶, P. Kaotira⁶, L. F. Lim⁶, A. Liounis⁶, C. Lorentson⁶, D. Lorenz⁶, J. Lyzhoft⁶², E. M. Mazarico⁶, R. Mink⁶, W. Moore⁶, M. Moreau⁶, S. Mullen⁶, J. Nagy⁶, G. Neumann⁶, J. Nuth⁶, D. Poland⁶, D. C. Reuter⁶, L. Rhoads⁶, S. Rieger⁶, D. Rowlands⁶, D. Sallitt⁶, A. Scroggins⁶, G. Shaw⁶, A. A. Simon⁶, J. Swenson⁶, P. Vasudeva⁶, M. Wasser⁶, R. Zellar⁶, J. Grossman⁶⁶, G. Johnston⁶⁶, M. Morris⁶⁶, J. Wendel⁶⁶, A. Burton⁶⁷, L. P. Keller⁶⁷, L. McNamara⁶⁷, S. Messenger⁶⁷, K. Nakamura-Messenger⁶⁷, A. Nguyen⁶⁷, K. Righter⁶⁷, E. Queen⁶⁸, K. Bellamy⁶⁹, K. Dill⁶⁹, S. Gardner⁶⁹, M. Giuntini⁶⁹, B. Key⁶⁹, J. Kissell⁶⁹, D. Patterson⁶⁹, D. Vaughan⁶⁹, B. Wright⁶⁹, R. W. Gaskell³, L. Le Corre³, J.-Y. Li³, J. L. Molaro³, E. E. Palmer³, M. A. Siegler³, P. Tricarico³, J. R. Weirich³, X.-D. Zou³, T. Ireland⁷⁰, K. Tait⁷¹, P. Bland⁷², S. Anwar⁷³, N. Bojorquez-Murphy⁷³, P. R. Christensen⁷³, C. W. Haberle⁷³, G. Mehall⁷³, K. Rios⁷³, I. Franchi⁷⁴, B. Rozitis⁷⁴, C. B. Beddingfield⁷⁵, J. Marshall⁷⁵, D. N. Brack¹², A. S. French¹², J. W. McMahon¹², D. J. Scheeres¹², E. R. Jawin⁹, T. J. McCoy⁹, S. Russell⁹, M. Killgore⁷⁶, W. F. Bottke¹⁰, V. E. Hamilton¹⁰, H. H. Kaplan¹⁰, K. J. Walsh¹⁰, J. L. Bandfield⁷⁷, B. C. Clark⁷⁷, M. Chodas⁷⁸, M. Lambert⁷⁸, R. A. Masterson⁷⁸, M. G. Daly², J. Freemantle², J. A. Seabrook², O. S. Barnouin¹, K. Craft¹, R. T. Daly¹, C. Ernst¹, R. C. Espiritu¹, M. Holdridge¹, M. Jones¹, A. H. Nair¹, L. Nguyen¹, J. Peachey¹, M. E. Perry¹, J. Plescia¹, J. H. Roberts¹, R. Steele¹, R. Turner¹, J. Backer⁷⁹, K. Edmundson⁷⁹, J. Mapel⁷⁹, M. Milazzo⁷⁹, S. Sides⁷⁹, C. Manzoni⁸⁰, B. May⁸⁰, M. Delbo⁸¹, G. Libourel¹¹, P. Michel¹¹, A. Ryan¹¹, F. Thuillet¹¹ and B. Marty⁸¹

¹⁹Aerospace Corporation, Chantilly, VA, USA. ²⁰Astronomical Institute, Charles University, Prague, Czech Republic. ²¹Atmospheric, Oceanic and Planetary Physics, University of Oxford, Oxford, UK. ²²Canadian Space Agency, Saint-Hubert, Quebec, Canada. ²³Catholic University of America, Washington, DC, USA. ²⁴Center for Astrophysics, Harvard University, Cambridge, MA, USA. ²⁵Center for Meteorite Studies, Arizona State University, Tempe, AZ, USA. ²⁶City University of New York, New York, NY, USA. ²⁷Colorado Center for Astrodynamics Research, University of Colorado, Boulder, CO, USA.

²⁸Commonwealth Scientific and Industrial Research Organisation (CSIRO), Canberra, Australian Capital Territory, Australia. ²⁹Department of Aerospace Engineering, Auburn University, Auburn, AL, USA. ³⁰Department of Aerospace Engineering, University of Maryland, College Park, MD, USA.

³¹Department of Astronomy and Steward Observatory, University of Arizona, Tucson, AZ, USA. ³²Department of Astronomy, Cornell University, Ithaca, NY, USA. ³³Department of Astronomy, University of Maryland, College Park, MD, USA. ³⁴Department of Earth and Planetary Sciences, University of Tennessee, Knoxville, TN, USA. ³⁵Department of Earth Sciences, University of Toronto, Toronto, Ontario, Canada. ³⁶Department of Earth, Atmospheric, and Planetary Sciences, Massachusetts Institute of Technology, Cambridge, MA, USA. ³⁷Department of Geography, University of Winnipeg, Winnipeg, Manitoba, Canada. ³⁸Department of Geological Sciences, Jackson School of Geosciences, University of Texas, Austin, TX, USA. ³⁹Department of Geology, Rowan University, Glassboro, NJ, USA. ⁴⁰Department of Geoscience, University of Calgary, Calgary, Alberta, Canada. ⁴¹Department of Geosciences, Stony Brook University, Stony Brook, NY, USA. ⁴²Department of Physics and Astronomy, Ithaca College, Ithaca, NY, USA. ⁴³Department of Physics and Astronomy, Northern Arizona University, Flagstaff, AZ, USA. ⁴⁴Department of Physics, University of Central Florida, Orlando, FL, USA. ⁴⁵Edge Space Systems, Greenbelt, MD, USA. ⁴⁶General Dynamics C4 Systems, Denver, CO, USA. ⁴⁷Hawai'i Institute of Geophysics and Planetology, University of Hawai'i at Mānoa, Honolulu, HI, USA. ⁴⁸Hokkaido University, Sapporo, Japan. ⁴⁹INAF-Astrophysical Observatory of Arcetri, Florence, Italy. ⁵⁰INAF-Osservatorio Astronomico di Padova, Padova, Italy. ⁵¹INAF-Osservatorio Astronomico di Roma, Rome, Italy. ⁵²Indigo Information Services, Tucson, AZ, USA.

⁵³Institut d'Astrophysique Spatiale, CNRS/Université Paris Sud, Orsay, France. ⁵⁴Institute for Planetary Materials, Okayama University-Misasa, Misasa, Japan. ⁵⁵Instituto de Astrofísica de Canarias and Departamento de Astrofísica, Universidad de La Laguna, Tenerife, Spain. ⁵⁶Jacobs Technology, Houston, TX, USA. ⁵⁷Jet Propulsion Laboratory, California Institute of Technology, Pasadena, CA, USA. ⁵⁸Kavli Institute for Astrophysics and Space Research, Massachusetts Institute of Technology, Cambridge, MA, USA. ⁵⁹Laboratory for Atmospheric and Space Physics, University of Colorado, Boulder, CO, USA. ⁶⁰LESIA, Observatoire de Paris, Université PSL, CNRS, Sorbonne Université, Univ. Paris Diderot, Sorbonne Paris Cité, Meudon, France.

⁶¹Macdonald, Dettwiler, and Associates, Brampton, Ontario, Canada. ⁶²Malin Space Science Systems, San Diego, CA, USA. ⁶³Mars Space Flight Facility, Arizona State University, Tempe, AZ, USA. ⁶⁴Mines ParisTech, Paris, France. ⁶⁵NASA Ames Research Center, Moffett Field, CA, USA. ⁶⁶NASA Headquarters, Washington, DC, USA. ⁶⁷NASA Johnson Space Center, Houston, TX, USA. ⁶⁸NASA Langley Research Center, Hampton, VA, USA. ⁶⁹NASA Marshall Space Flight Center, Huntsville, AL, USA. ⁷⁰Research School of Earth Sciences, Australian National University, Canberra, Australian Capital Territory, Australia.

⁷¹Royal Ontario Museum, Toronto, Ontario, Canada. ⁷²School of Earth and Planetary Sciences, Curtin University, Perth, Western Australia, Australia. ⁷³School of Earth and Space Exploration, Arizona State University, Tempe, AZ, USA. ⁷⁴School of Physical Sciences, The Open University, Milton Keynes, UK. ⁷⁵SETI Institute, Mountain View, CA, USA. ⁷⁶Southwest Meteorite Laboratory, Payson, AZ, USA. ⁷⁷Space Science Institute, Boulder, CO, USA.

⁷⁸Space Systems Laboratory, Department of Aeronautics and Astronautics, Massachusetts Institute of Technology, Cambridge, MA, USA. ⁷⁹US Geological Survey Astrogeology Science Center, Flagstaff, AZ, USA. ⁸⁰London Stereoscopic Company, London, UK. ⁸¹Université de Lorraine, Nancy, France.